The Astrophysical Journal, 884:113 (11pp), 2019 October 20 https://doi.org/10.3847/1538-4357/ab3a33

The Age Evolution of the Radio Morphology of Supernova Remnants

Jennifer N. Stafford[1], Laura A. Lopez[1,2,3], Katie Auchettl[2,4], and Tyler Holland-Ashford[1]
[1] Department of Astronomy, The Ohio State University, 140 W. 18th Ave., Columbus, Ohio 43210, USA; stafford.205@osu.edu
[2] Center for Cosmology and AstroParticle Physics, The Ohio State University, 191 W. Woodruff Ave., Columbus, OH 43210, USA
[3] Niels Bohr Institute, University of Copenhagen, Blegdamsvej 17, DK-2100 Copenhagen, Denmark
[4] Department of Physics, The Ohio State University, 191 W. Woodruff Ave., Columbus, OH 43210, USA
Received 2018 August 24; revised 2019 August 2; accepted 2019 August 9; published 2019 October 16

Abstract

Recent hydrodynamical models of supernova remnants (SNRs) demonstrate that their evolution depends heavily on the inhomogeneities of the surrounding medium. As SNRs expand, their morphologies are influenced by the nonuniform and turbulent structure of their environments, as reflected in their radio continuum emission. In this paper, we measure the asymmetries of 96 SNRs in radio continuum images from three surveys of the Galactic plane and compare these results to the SNRs' radii, which we use as a proxy for their age. We find that larger (older) SNRs are more elliptical/elongated and more mirror asymmetric than smaller (younger) SNRs, though the latter vary in their degrees of asymmetry. This result suggests that SNR shells become more asymmetric as they sweep up the interstellar medium (ISM), as predicted in hydrodynamical models of SNRs expanding in a multiphase or turbulent ISM.

Key words: ISM: supernova remnants – radio continuum: ISM – supernovae: general

1. Introduction

Synchrotron radiation is produced by electrons that are accelerated at the shocks of supernova remnants (SNRs) and interact with the local magnetic field (see, e.g., Berezhko & Völk 2004). This emission dominates at radio wavelengths, particularly at lower frequencies (e.g., 1.4 GHz) where thermal bremsstrahlung contributes less to the spectrum. Radio continuum surveys are the primary means by which new SNRs are identified (see, e.g., Chomiuk & Wilcots 2009 and references therein). At present, 295 objects have been classified as SNRs in the Milky Way (Green 2017), and 95% of these are radio sources (Dubner & Giacani 2015).

Historically, SNRs have been classified based on their nonthermal radio shells (e.g., Milne & Hill 1969). After many SNRs were resolved at radio wavelengths, astronomers began to categorize them based on their morphologies (e.g., Green 1984). The categories most commonly used are shell-type, composite, and mixed-morphology. Shell-type SNRs are those with limb-brightened radio shell emission (e.g., SN 1006: Winkler et al. 2014, G1.9+0.3: De Horta et al. 2014) and 79% of Galactic SNRs fall into this group (Dubner & Giacani 2015). Composite SNRs are ones that have both the shell and the center-filled emission from a pulsar wind nebula (e.g., MSH 15–56: Dickel et al. 2000, Vela SNR: Dodson et al. 2003). Additionally, X-ray imaging led to another class of SNRs called mixed-morphology or thermal-composite (Rho & Petre 1998; Lazendic & Slane 2006; Shelton et al. 2004) that have radio shells with center-filled X-rays (e.g., W44, IC443: Kawasaki et al. 2005).

Barrel-shaped or bilateral SNRs, a subgroup of shell-type SNRs, are characterized by an axisymmetric morphology with two bright limbs. Gaensler (1998) analyzed a sample of bilateral SNRs at radio frequencies and showed that their axes tended to be aligned with the Galactic plane. More recently, West et al. (2016) investigated all Milky Way bilateral SNRs, and they showed that a simple model of SNRs expanding into an ambient Galactic magnetic field could reproduce the observed radio morphologies.

To quantify the complex and varied morphologies of SNRs, Lopez et al. (2009b) developed and applied several mathematical tools. Using the power-ratio method (PRM), Lopez et al. (2009a, 2011) showed that the thermal X-ray emission of Type Ia SNRs is more symmetric and circular than that of core-collapse SNRs. Subsequently, Peters et al. (2013) extended this approach to infrared images of SNRs and found similar results as in the X-ray. Recently, Holland-Ashford et al. (2017) used the PRM to compare the SNR soft X-ray morphologies to neutron star velocities and showed that the neutron stars are moving opposite to the bulk of the supernova (SN) ejecta in many sources. For a detailed summary of these results and those of other groups, see Lopez & Fesen (2018).

In this paper, we investigate the radio morphologies of SNRs in the Milky Way to examine how asymmetries evolve with size and age. SNRs are observable for $\sim 10^4$–10^5 years at radio wavelengths (Sarbadhicary et al. 2017), and their morphologies are shaped by interactions with the surrounding medium (e.g., Zhang & Chevalier 2018) and by the magnetic field (e.g., Orlando et al. 2007; West et al. 2017).

This paper is structured as follows. In Section 2, we describe the radio data and introduce our sample of Galactic SNRs. Section 3 outlines the PRM, which we employ to measure the asymmetries of the sources. Finally, Section 4 presents our results and discusses the implications regarding SNR evolution.

2. Data and Sample

Our sample is comprised of 96 SNRs imaged in three surveys/catalogs of the Galactic plane: the HI, OH, Recombination Line (THOR) Survey (Beuther et al. 2016), the Canadian Galactic Plane Survey (CGPS; Kothes et al. 2006), and the Molonglo Observatory Synthesis Telescope (MOST) SNR catalog (Whiteoak & Green 1996) We describe the data and the sample selection from each survey below.

The final sample includes 59 SNRs with constraints on their explosive origins (5 Type Ia SNRs, 54 core-collapse SNRs). 63 out of the 96 SNRs have distance measurements in the literature, as listed in Tables 1–3. Distances are determined

Table 1
List of SNRs in Our Sample from THOR

No.	Source[a]	Alternate Names	Distance[b] (kpc)	Evidence of Explosion Type[c]	P_1/P_0 ($\times10^{-5}$)	P_2/P_0 ($\times10^{-7}$)	P_3/P_0 ($\times10^{-7}$)	References
1	G15.9+0.2	⋯	8.5[b]	N	$84.9^{+9.0}_{-7.2}$	$8.50^{+6.70}_{-6.37}$	$4.90^{+2.46}_{-2.83}$	1
2	G16.7+0.1[a]	⋯	10	N	3.01 ± 1.3	$18.7^{+7.3}_{-8.3}$	$2.79^{+1.84}_{-1.82}$	2
3	G18.1−0.1[a]	⋯	6.4 ± 0.2	E	$95.9^{+1.5}_{-1.4}$	326 ± 9	$5.25^{+0.51}_{-0.64}$	3
4	G18.8+0.3[a]	Kes 67	13.8 ± 4.0	E	240^{+1}_{-2}	1119^{+12}_{-13}	149 ± 2	3,4
5	G20.0−0.2	⋯	11.2 ± 0.3	E, N	27.3 ± 0.7	$43.9^{+3.3}_{-2.8}$	$2.71^{+0.57}_{-0.47}$	3
6	G20.4+0.1	⋯	7.8	E, N	74.9 ± 2.9	259^{+19}_{-18}	$33.4^{+2.4}_{-2.6}$	5
7	G21.5−0.1	⋯	8.5[b]	⋯	$13.1^{+2.2}_{-2.7}$	$16.2^{+12.5}_{-11.7}$	$2.74^{+1.62}_{-1.94}$	⋯
8	G21.8−0.6[a]	Kes 69	$5.2^{+0.0}_{-0.3}$	E	370 ± 1	760 ± 5	100 ± 1	6, 7
9	G22.7−0.2	⋯	4.4 ± 0.4	E	$36.4^{+0.3}_{-0.2}$	162 ± 2	$6.03^{+0.17}_{-0.20}$	8
10	G23.3−0.3[a]	W41	4.4 ± 4	E	$96.5^{+0.4}_{-0.3}$	951^{+5}_{-4}	94.5 ± 7	9, 10
11	G27.4+0.0[a]	Kes 73	5.8 ± 0.3	N, A	16.2 ± 0.4	85.2^{+4}_{-3}	$3.64^{+0.38}_{-0.32}$	3, 11
12	G28.6−0.1	⋯	9.6 ± 0.3	E	$3.82^{+0.21}_{-0.23}$	819 ± 12	189 ± 3	5
13	G29.6+0.1[a]	⋯	10.0 ± 5.0	N	$5.95^{+1.13}_{-1.12}$	$81.3^{+12.4}_{-15.9}$	$17.2^{+3.0}_{-3.4}$	12
14	G31.9+0.0[a]	3C 391	7.1 ± 0.4	E, A	63.9 ± 0.3	240^{+3}_{-2}	$6.54^{+0.17}_{-0.18}$	13, 14
15	G32.4+0.1[a]	⋯	17	E	$48.5^{+4.9}_{-5.4}$	170^{+28}_{-34}	$92.5^{+14.6}_{-14.2}$	14, 15
16	G32.8−0.1[a]	Kes 78	4.8	E, N	$87.9^{+1.3}_{-1.6}$	4005^{+53}_{-50}	$94.1^{+3.0}_{-2.5}$	16, 17
17	G33.2−0.6[a]	⋯	8.5[b]	⋯	180^{+3}_{-4}	106 ± 8	$0.34^{+0.25}_{-0.24}$	–
18	G33.6+0.1[a]	Kes 79	3.5 ± 0.3	N, A	$96.8^{+0.8}_{-0.9}$	$3.70^{+0.60}_{-0.50}$	24.2 ± 0.6	3,18,19
19	G34.7−0.4[a]	W44	3.0 ± 0.3	E, N, A	$5.28^{+0.04}_{-0.03}$	575 ± 2	27.0 ± 0.2	3,20,21
20	G35.6−0.4	⋯	3.6 ± 0.4	E	$5.21^{+0.23}_{-0.20}$	538 ± 9	$5.28^{+0.47}_{-0.53}$	22
21	G36.6−0.7	⋯	8.5[b]	⋯	190 ± 3	825 ± 22	$34.8^{+2.9}_{-2.8}$	⋯
22	G49.2−0.7[a]	W51C	5.4 ± 0.6	E, A	$8.56^{+0.08}_{-0.09}$	726^{+2}_{-3}	50.7 ± 0.3	23, 24

Notes.
[a] Denotes SNRs with evidence of interaction with a molecular cloud: G16.7+0.1: Green et al. (1997) (G97); Reynoso & Mangum (2000); Hewitt et al. (2008; H08); Kilpatrick et al. (2016; K16); G18.1−0.1: Froebrich et al. (2015; F15); G18.8+0.3: Dubner et al. (2004); Tian et al. (2007b); G21.8−0.6: G97; H08; Zhou et al. (2009); Hewitt et al. (2009); F15; G23.3−0.3: Frail et al. (2013) G27.4+0.0: F15, K16; G29.6+0.1: K16; G31.9+0.0: Frail et al. (1996); Reach & Rho (1999); Reach et al. (2002), H08, F15, K16; G32.4+0.1: K16; G32.8−0.1: Koralesky et al. (1998); Zhou & Chen (2011); F15; G33.2−0.6: F15, K16; G33.6+0.1: K16, Zhou et al. (2016a); G34.7−0.4: Claussen et al. (1997), Seta et al. (1998), Reach et al. (2005); H08; G49.2−0.7: G97; Koo & Moon (1997); H08.
[b] Denotes an SNR with an assumed distance of 8.5 kpc (the International Astronomical Union recommended distance to the Galactic center) because the source does not have good constraints on its distance.
[c] Evidence of explosion type: N = neutron star detection; E = environment suggestive of core-collapse SNe (e.g., molecular cloud interaction, nearby HII regions); A = metal abundances from X-ray observations are consistent with core-collapse SNe.
References. (1) Reynolds et al. (2006); (2) Helfand et al. (2003); (3) Ranasinghe & Leahy (2018b); (4) Tian et al. (2007b); (5) Ranasinghe & Leahy (2018a); (6) Zhou et al. (2009); (7) Leahy & Tian (2008); (8) Su et al. (2014); (9) Su et al. (2015); (10) Frail et al. (2013); (11) Vasisht & Gotthelf (1997); (12) Vasisht et al. (2000); (13) Ranasinghe & Leahy (2017); (14) Kilpatrick et al. (2016); (15) Yamaguchi et al. (2004); (16) Zhou & Chen (2011); (17) Bamba et al. (2016b); (18) Sato et al. (2016); (19) Auchettl et al. (2014); (20) Uchida et al. (2012); (21) Radhakrishnan et al. (1972); (22) Zhu et al. (2013); (23) Tian & Leahy (2013); (24) Sasaki et al. (2014).

primarily through HI absorption spectra (e.g., Leahy et al. 2014) and/or via kinematic velocities of associated molecular clouds (e.g., Ranasinghe & Leahy 2017, 2018a). The error bars on the distances in Tables 1–3 reflect the uncertainties quoted in the literature for each measurement. If no error bars are given for the distances in Tables 1–3, then the references did not assess the uncertainties in those values.

2.1. THOR Survey

The THOR Survey used the Karl G. Jansky Very Large Array[5] to observe the radio continuum in 6 bands (from 1 to 2 GHz), the HI 21 cm line, four OH lines, and radio recombination lines over the first Galactic Quadrant (Galactic longitudes from $14.^{\circ}5 < l < 67.^{\circ}25$ and latitudes of $|b| \leqslant 1.^{\circ}25$[6]). We opted to analyze the 1.4 GHz radio data, because 95% of SNRs are detected at this frequency (Chomiuk & Wilcots 2009; Dubner & Giacani 2015). The spatial resolution of the THOR data is 20″.

In the area of the THOR survey, 34 SNRs have been identified (Green 2017), and all were fully imaged. However, we excluded 12 SNRs due to substantial artifacts in the data (e.g., G15.4+0.1, G31.5−0.6) or because their radio emission is dominated by a pulsar wind nebula rather than the synchrotron from their shells (e.g., G21.5−0.9, Kes 75). The THOR sample of 22 SNRs is listed in Table 1, and the images of the SNRs are presented in Figure 1. The THOR SNRs have a range in radii from 1.′5 to 20′ (Green 2017).

Out of the 22 THOR SNRs, 19 are likely from core-collapse explosions, based on the presence of neutron stars, metal abundances, and/or their dense, star-forming environments (see Table 1). The other three have insufficient data to characterize explosion type (G21.5−0.1, G33.2−0.6, and G36.6−0.7), but given their location within the Galactic plane, they may also be from core-collapse SNe. As many Type Ia SNRs are found at high galactic latitudes (e.g., *Kepler*, SN 1006), it is not surprising that the THOR sample has no known Type Ia sources. We note that two of the THOR SNRs

[5] http://www.mpia.de/thor
[6] Only the first half of the survey data is publicly available currently, which covers longitudes from $14.^{\circ}5$ to $37.^{\circ}9$ and $47.^{\circ}1$ to $51.^{\circ}2$.

Table 2
List of SNRs in Our Sample from CGPS

No.	Source[a]	Alternate Names	Distance[b] (kpc)	Evidence of Explosion Type[c]	P_1/P_0 ($\times10^{-5}$)	P_2/P_0 ($\times10^{-7}$)	P_3/P_0 ($\times10^{-7}$)	References
23	G65.1+0.6[d]	⋯	$9.2^{+0.4}_{-0.2}$	N, E	$50.1^{+0.9}_{-1.0}$	1748^{+19}_{-18}	79.2^{+2}_{-3}	1
24	G67.7+1.8	⋯	8.5[b]	A	$59.9^{+1.4}_{-1.2}$	$16.9^{+2.7}_{-2.4}$	48.4±2	2
25	G69.0+2.7	CTB 80	$1.5^{+0.6}_{-0.4}$	N	6040±38	20060^{+181}_{-186}	2073^{+24}_{-22}	3, 4
26	G69.7+1.0	⋯	8.5[b]	⋯	11.7±0.4	67.6±2.8	$4.16^{+0.37}_{-0.40}$	⋯
27	G73.9+0.9[d]	⋯	$1.3^{+0.7}_{-0.8}$	E	22.6±0.2	$25.4^{+8.4}_{-8.3}$	12.4±0.3	5
28	G78.2+2.1	γ Cygni SNR	$2.0^{+0.6}_{-0.3}$	N	77.1±0.1	1139^{+1}_{-2}	93.3±0.2	6, 7
29	G84.2−0.8	⋯	6.0 ± 0.2	⋯	780^{+7}_{-8}	5151^{+6}_{-5}	$87.3^{+2.8}_{-3.0}$	8
30	G85.4+0.7	⋯	3.5 ± 1.0	⋯	792^{+9}_{-8}	1429±3	$88.9^{+3.7}_{-4.2}$	9
31	G93.7−0.2	CTB 104A	1.5 ± 0.2	⋯	329^{+1}_{-1}	230±3	221±2	10
32	G94.0+1.0[d]	3C 434.1	4.5 ± 1.5	E	126±1	489±2	5.08±0.14	11, 12
33	G106.3+2.7	⋯	$0.8^{+1.2}_{-0.1}$	N, E	$50.0^{+0.7}_{-0.6}$	6010^{+4}_{-3}	104±2	13
34	G109.1−1.0[d]	CTB 109	3.2 ± 0.2	N, E	30.7±0.1	739^{+3}_{-2}	$12.1^{+0.2}_{-0.1}$	14
35	G114.3+0.3	⋯	$0.7^{+0.9}_{-0.0}$	N	53.1±0.2	128±1	$1.66^{+0.07}_{-0.06}$	15, 16
36	G116.5+1.1	⋯	1.6 ± 0.6	⋯	24.3±0.3	1458±9	$12.6^{+0.5}_{-0.4}$	15
37	G116.9+0.2	CTB 1	$1.6^{+1.5}_{-0.0}$	A	87.7±0.4	331^{+3}_{-2}	10.6±0.3	15, 17
38	G120.1+1.4[a]	Tycho	$2.4^{+2.6}_{-0.9}$	A, L	8.00±0.03	0.09±0.01	0.65±0.01	18, 19
39	G127.1+0.5[d]	R 5	1.2 ± 0.1	E	20.6±0.1	124±1	10.3±0.2	20
40	G132.7+1.3[d]	HB 3	2.2 ± 0.2	E, A	$308^{+0.5}_{-0.4}$	583±2	74.0±0.4	17, 21
41	G160.9+2.6	HB 9	$0.8^{+1.0}_{-0.4}$	⋯	47.7±0.1	364±1	0.33±0.02	22
42	G166.0+4.3[d]	VRO 42.05.01	4.5 ± 1.5	E	$1.13^{+0.09}_{-0.10}$	745^{+11}_{-9}	$63.8^{+1.4}_{-1.4}$	23

Notes.
[a] Denotes SNRs thought to be from SNe Ia.
[b] Denotes an SNR with an assumed distance of 8.5 kpc (the International Astronomical Union recommended distance to the Galactic center) because the source does not have good constraints on its distance.
[c] Evidence of explosion type: N = neutron star detection; E = environment suggestive of core-collapse SNe (e.g., molecular cloud interaction, nearby HII regions); A = metal abundances from X-ray observations; L = light echo spectrum.
[d] Denotes SNRs with evidence of interaction with a molecular cloud: G65.1+0.6: F15; G73.9+0.9: Zdziarski et al. (2016); G94.0+1.0: Jeong et al. (2013); G109.1−1.0: Sasaki et al. (2006); G127.1+0.5: Zhou et al. (2014); G132.7+1.3: K16, Zhou et al. (2016b).
References. (1) Tian & Leahy (2006); (2) Hui & Becker (2009); (3) Li et al. (2005); (4) Leahy & Ranasinghe (2012); (5) Lozinskaya et al. (1993); (6) Leahy et al. (2013); (7) Hui et al. (2015); (8) Leahy & Green (2012); (9) Jackson et al. (2008); (10) Uyaniker et al. (2002); (11) Foster (2005); (12) Jeong et al. (2013); (13) Kothes et al. (2001); (14) Kothes & Foster (2012); (15) Yar-Uyaniker et al. (2004); (16) Kulkarni et al. (1993); (17) Lazendic & Slane (2006);(18) Tian & Leahy (2011); (19) Krause et al. (2008); (20) Leahy & Tian (2006); (21) Routledge et al. (1991); (22) Leahy & Tian (2007); (23) Landecker et al. (1989).

considered in this work (Kes 69 and G28.6−0.1) were in the bilateral sample analyzed by West et al. (2016).

2.2. CGPS

The CGPS surveyed atomic hydrogen and the radio continuum using the Dominion Radio Astrophysical Observatory (Taylor et al. 2003). CGPS data is available in 5° × 5° mosaics[7] and covers longitudes of $52° < l < 192°$ and latitudes of $-3.^{\circ}5 < b < 5.^{\circ}5$. Kothes et al. (2006) cataloged the known and candidate Galactic SNRs in the CGPS fields, with a final sample of 36 sources. For our work, we analyzed the 1.42 GHz radio continuum CGPS data, which has 18″ pixels and 1′ resolution.

We downloaded the CGPS data and examined the 36 SNRs identified by Kothes et al. (2006). We excluded 16 SNRs from the sample because of bright PWNe dominating their emission (e.g., G65.7+1.2 [DA 495], G130.7+3.1 [3C 58]), contaminating emission from foreground or nearby sources (e.g., G83.0−0.3), or low signal (e.g., G126.2+1.6). In addition, one source (G84.9+0.5) is now classified as a HII region (Foster et al. 2007), so it is not considered. The CGPS sample of 20 SNRs is listed in Table 2, and the images of the SNRs are presented in Figure 2. The CGPS SNRs span a range in radii of 7′–76′.

Of the 20 SNRs, 13 are classified as core-collapse explosions, based on detections of neutron stars, metal abundances, and/or interactions with dense, star-forming environments. One SNR (G120.1+1.4 [Tycho]) is associated with SN 1572 and known to have originated from a Type Ia explosion based on its light echo spectrum (Krause et al. 2008). The other six SNRs have insufficient data to characterize their explosion types. We note that four of the CGPS SNRs considered in this work (G65.1+0.6, G116.9+0.2 [CTB 1], G127.1+0.5, G166.0+4.3 [VRO 42.05.01) were among the bilateral sample of West et al. (2016).

2.3. MOST

The MOST Galactic plane survey observed the radio continuum at 0.843 GHz and covers longitudes of $245° < l < 355°$ and latitudes of $|b| \leqslant 1.^{\circ}5$. Each field of the survey covers an area of 70′ × 70′ and achieved spatial resolutions of 43″. Whiteoak & Green (1996) constructed the MOST SNR catalog (MSC), which included 57 known SNRs (the category called MSC.A in Whiteoak & Green 1996) and 18 new SNRs (the category called MSC. B in Whiteoak & Green 1996).

[7] http://www.cadc-ccda.hia-iha.nrc-cnrc.gc.ca/en/cgps/

Table 3
List of SNRs in Our Sample from MOST

No.	Source[a]	Alternate Names	Distance[c] (kpc)	Evidence of Explosion Type[b]	P_1/P_0 ($\times10^{-3}$)	P_2/P_0 ($\times10^{-7}$)	P_3/P_0 ($\times10^{-7}$)	References
43	G289.7−0.3	⋯	8.5[d]	⋯	$71.8^{+0.4}_{-0.3}$	971±5	0.04±0.01	
44	G290.1−0.8[c]	MSH 11−61A	7.0 ± 1.0	N, E, A	23.8±0.1	230±1	9.40±0.07	1, 2, 3
45	G294.1−0.0	⋯	8.5[d]	⋯	788^{+11}_{-10}	6189^{+134}_{-121}	2376^{+37}_{-42}	
46	G296.1−0.5	⋯	3.0 ± 1.0	A	523±2	2578^{+16}_{-19}	688^{+5}_{-6}	4, 5
47	G296.8−0.3	⋯	9.6 ± 0.6	⋯	1134±3	3630±17	373±3	6
48	G298.6−0.0[c]	⋯	8.5[d]	E	57.4±0.1	1285^{+4}_{-3}	121±1	7
49	G299.6−0.5	⋯	8.5[d]	⋯	115±1	$67.3^{+3.0}_{-2.6}$	$77.7^{+1.3}_{-1.5}$	
50	G301.4−1.0	⋯	8.5[d]	⋯	$79.6^{+1.8}_{-2.0}$	2422±1	591^{+14}_{-13}	
51	G302.3+0.7[c]	⋯	8.5[d]	E	$48.2^{+0.7}_{-0.6}$	946±10	567^{+3}_{-4}	8
52	G304.6+0.1[c]	Kes 17	$9.7^{+4.3}_{-1.7}$	E, A	30.1±0.1	137±1	6.71±0.03	9, 10
53	G308.1−0.7	⋯	8.5[d]	⋯	12.5±0.4	$74.8^{+3.0}_{-3.4}$	141±2	
54	G308.8−0.1	⋯	$6.9^{+8.1}_{-2.9}$	N	447±1	2612^{+7}_{-6}	221±1	11
55	G309.2−0.6	⋯	4.0 ± 2.0	⋯	4.93±0.09	2278^{+6}_{-5}	$65.5^{+3.3}_{-3.1}$	12
56	G309.8+0.0	⋯	8.5[d]	⋯	503±2	1237^{+17}_{-16}	1418^{+7}_{-8}	⋯
57	G310.6−0.3	Kes 20B	8.5[d]	⋯	228±1	1005±6	47.8±0.6	⋯
58	G310.8−0.4	Kes 20A	13.7	E	209±1	4222^{+9}_{-7}	509±2	13, 14
59	G311.5−0.3[c]	⋯	14.8	E	1.92±0.02	$9.75^{+0.14}_{-0.16}$	0.28±0.02	14
60	G312.4−0.4[c]	⋯	$6.0^{+8.0}_{-0.0}$	E	441±1	172^{+4}_{-3}	151±1	15
61	G315.4−2.3[a]	RCW 86	$2.5^{+0.3}_{-0.2}$	E, A	116±6	4379±2	2098^{+7}_{-6}	16, 17, 18
62	G316.3−0.0	MSH 14−57	7.2 ± 0.6	⋯	$2.28^{+0.05}_{-0.04}$	228^{+1}_{-2}	61.1±0.3	10
63	G317.3−0.2	⋯	8.5[d]	⋯	267±1	7315±15	781±3	
64	G318.2+0.1	⋯	8.5[d]	⋯	$66.6^{+0.9}_{-1.0}$	2537^{+21}_{-23}	120^{+4}_{-3}	
65	G321.9−0.3	⋯	$6.5^{+3.5}_{-1.0}$	N	289±2	1588^{+18}_{-16}	$85.9^{+1.9}_{-2.2}$	19
66	G321.9−1.1	⋯	8.5[d]	⋯	2051^{+25}_{-23}	7226^{+122}_{-155}	3639±6	
67	G322.5−0.1	⋯	8.5[d]	N	$50.0^{+0.5}_{-0.6}$	257^{+5}_{-4}	112±1	20
68	G323.5+0.1	⋯	8.5[d]	⋯	$21.4^{+0.1}_{-0.2}$	460±3	$51.6^{+0.5}_{-0.4}$	⋯
69	G326.3−1.8	MSH 15−56	4.1 ± 0.7	N	35.6±0.1	114±1	0.60±0.02	16, 21
70	G327.1−1.1	⋯	8.5 ± 0.5	N	45.3±0.3	126^{+1}_{-2}	11.8±0.2	22
71	G327.4+0.4	Kes 27	$4.3^{+1.1}_{-0.0}$	N	237±1	1194^{+5}_{-4}	113±1	23, 24
72	G327.4+1.0	⋯	8.5[d]	⋯	79.2 ± 0.4	1040^{+5}_{-4}	240 ± 1	⋯
73	G329.7+0.4	⋯	8.5[d]	E	106 ± 1	$5.63^{+0.05}_{-0.04}$	$64.6^{+0.8}_{-0.7}$	⋯
74	G330.2+1.0	⋯	$4.9^{+5.0}_{-0.0}$	N	144 ± 1	114 ± 1	$24.1^{+0.2}_{-0.3}$	23, 25
75	G332.0+0.2	⋯	8.5[d]	⋯	0.17 ± 0.01	770 ± 2	60.6 ± 0.3	⋯
76	G332.4+0.1[c]	Kes 32	$7.5^{+3.5}_{-0.9}$	E	18.2 ± 0.1	1658 ± 2	142 ± 1	26
77	G332.4−0.4[c]	RCW 103	$3.3^{+1.3}_{-0.2}$	N, E, A	$20.2^{+2.8}_{-3.2}$	12.8 ± 0.1	4.29 ± 0.02	27, 28
78	G335.2+0.1	⋯	1.8	N	$19.8^{+10.2}_{-12.0}$	43.7 ± 0.6	91.1 ± 0.4	29, 30
79	G336.7+0.5	⋯	8.5[d]	⋯	534^{+62}_{-54}	2092 ± 6	241 ± 1	⋯
80	G337.2−0.7◇	⋯	2.0 ± 0.5	A	4.43 ± 0.02	$3.71^{+0.07}_{-0.08}$	2.75 ± 0.03	31, 32
81	G337.3+1.0	Kes 40	8.5[d]	⋯	2.15 ± 0.02	165 ± 1	$34.7^{+0.2}_{-0.1}$	⋯
82	G337.8−0.1[c]	Kes 41	11.0	E	5.51 ± 0.02	1017 ± 1	$20.4^{+0.1}_{-0.1}$	33
83	G340.4+0.4	⋯	8.5[d]	⋯	93.0 ± 0.2	188 ± 1	68.4 ± 0.4	⋯
84	G340.6+0.3	⋯	15.0	⋯	39.1 ± 0.2	126 ± 1	11.6 ± 0.1	33
85	G341.9−0.3	⋯	8.5[d]	⋯	204 ± 1	385 ± 3	$24.3^{+0.3}_{-0.4}$	⋯
86	G342.0−0.2	⋯	8.5[d]	⋯	50.0 ± 0.2	203 ± 2	$9.25^{+0.17}_{-0.21}$	⋯
87	G342.1+0.9	⋯	8.5[d]	⋯	13.0 ± 0.2	218^{+3}_{-2}	2.98 ± 0.16	⋯
88	G343.1−0.7	⋯	8.5[d]	⋯	$34.4^{+0.2}_{-0.3}$	2504 ± 9	516 ± 3	⋯
89	G344.7−0.1◇	⋯	$6.3^{+7.7}_{-0.1}$	A	52.9 ± 0.2	$63.7^{+0.6}_{-0.7}$	$14.3^{+0.1}_{-0.2}$	34, 35
90	G346.6−0.2[c]	⋯	11	E	4.48 ± 0.04	26.1 ± 0.3	$5.38^{+0.06}_{-0.07}$	36
91	G348.7+0.3	CTB 37B	13.2 ± 0.2	N	578 ± 1	$88.3^{+3.0}_{-2.7}$	$43.5^{+0.3}_{-0.4}$	37, 38
92	G351.2+0.1	⋯	8.5[d]	⋯	41.4 ± 0.1	333 ± 1	19.7 ± 0.1	
93	G351.7+0.8	⋯	13.2 ± 0.5	⋯	131 ± 1	261 ± 2	2.88 ± 0.14	39
94	G351.9−0.9	⋯	8.5[d]	⋯	270 ± 1	533 ± 5	92.2 ± 1.1	
95	G352.7−0.1[a]	⋯	$7.5^{+0.9}_{-0.7}$	A	0.07 ± 0.01	218 ± 1	36.1 ± 0.1	40, 41
96	G354.8−0.8	⋯	8.5[d]	⋯	11.7 ± 0.3	3750 ± 2	520 ± 3	

Notes.
[a] Denotes SNRs thought to be from SNe Ia.
[b] Evidence of Explosion Type: N = neutron star detection; E = environment suggestive of core-collapse SNe (e.g., molecular cloud interaction, nearby HII regions); A = metal abundances from X-ray observations; L = light echo spectrum.
[c] Denotes SNRs with evidence of interaction with a molecular cloud: G290.1−0.8: Filipovic et al. (2005); G298.6−0.0: Acero et al. (2016); G302.3+0.7: Frail et al. (1996) (F96); G304.6+0.1: F96; Hewitt et al. (2009); G311.5−0.3: Andersen et al. (2011); G312.4−0.4: F96; G332.4+0.1: F96; G332.4−0.4: F96; Paron et al. (2006); G337.0−0.1: F96; G337.8−0.1: Koralesky et al. (1998); Zhang et al. (2015); G346.6−0.2: Koralesky et al. (1998); Hewitt et al. (2009); Andersen et al. (2011); G348.5+0.1: F96, Reynoso & Mangum (2000).
[d] Denotes an SNR with an assumed distance of 8.5 kpc (the International Astronomical Union recommended distance to the Galactic center) because the source does not have good constraints on its distance.
References. (1) Reynoso et al. (2006); (2) Auchettl et al. (2015); (3) Kaspi et al. (1997); (4) Castro et al. (2011); (5) Longmore et al. (1977); (6) Gaensler et al. (1998); (7) Bamba et al. (2016a); (8) Frail et al. (1996); (9) Washino et al. (2016); (10) Caswell et al. (1975); (11) Caswell et al. (1992);(12) Rakowski et al. (2001); (13) Reach et al. (2006); (14) Andersen et al. (2011); (15) Doherty et al. (2003); (16) Rosado et al. (1996); (17) Sollerman et al. (2003); (18) Williams et al. (2011); (19) Stewart et al. (1993); (20) Whiteoak & Green (1996); (21) Temim et al. (2013); (22) Sun et al. (1999); (23) McClure-Griffiths et al. (2001); (24) Chen et al. (2008); (25) Park et al. (2009); (26) Vink (2004); (27) Reynoso et al. (2004); (28) Frank et al. (2015); (29) Kaspi et al. (1996); (30) Eger et al. (2011); (31) Rakowski et al. (2006); (32) Yamaguchi et al. (2014); (33) Kothes & Dougherty (2007); (34) Giacani et al. (2011); (35) Yamaguchi et al. (2012); (36) Koralesky et al. (1998); (37) Tian & Leahy (2012); (38) Halpern & Gotthelf (2010); (39) Tian et al. (2007a); (40) Giacani et al. (2009); (41) Sezer & Gök (2014).

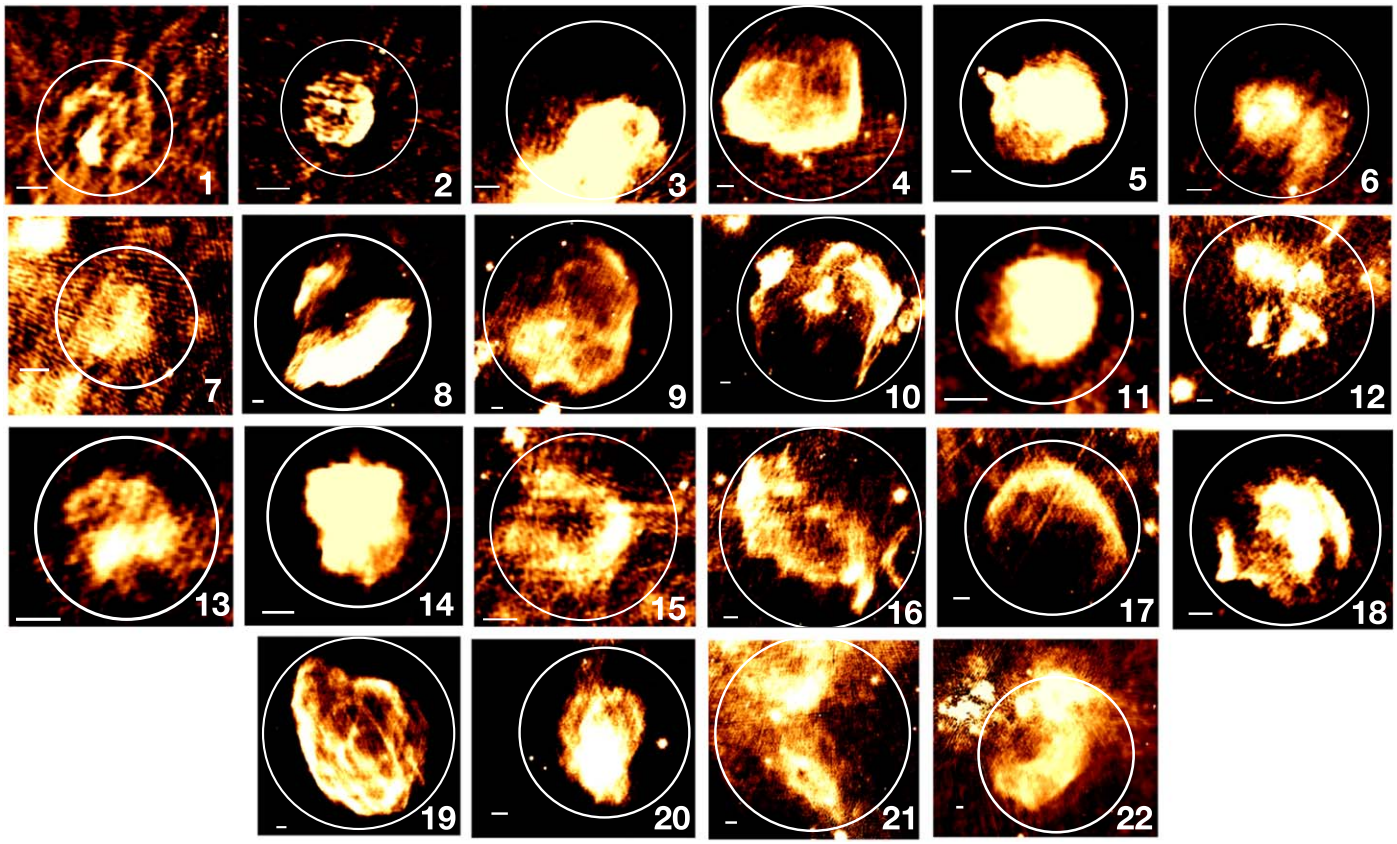

Figure 1. Radio continuum (1.4 GHz) images of 22 SNRs from the HI, OH, Recombination Line (THOR) Survey with the JVLA (Beuther et al. 2016). The SNRs range in radius of 1.′5–20′ (Green 2017). The extents of the sources are marked with white circles, and the white scale bar represents 2′. The numbers correspond to those in column 1 of Table 1.

We downloaded the MOST data and examined the 75 SNRs from MSC.A and MSC.B. As with the THOR and CGPS samples, we excluded the MSC SNRs with emission dominated by PWNe (e.g., G291.0−0.1, G320.4−1.2, G338.3−0.0), with contamination from nearby sources (e.g., G315.4−2.3, G320.6−1.6, G349.2−0.1), or that were not sufficiently detected or resolved (e.g., G298.5−0.3, G345.7−0.2, G349.7+0.2). The final sample of 54 MSC SNRs analyzed in this work are listed in Table 3, and their images are given in Figure 3. The MSC SNRs have radii of 3′–23′.

Compared to the THOR and CGPS observed SNRs, the MSC SNRs in our sample have fewer constraints on their explosive origins, with 28 SNRs lacking observational indications of SN type. Twenty-two MSC SNRs show evidence of being from core-collapse explosions, and four MSC SNRs are thought to be from SNe Ia (RCW 86, G337.2−0.7, G344.7−0.1, G352.7−0.1; see references in Table 3). Seven of the MSC SNRs in our sample (G302.3+0.7, G317.3−0.2, G321.9−0.3, G327.4+1.0, G332.0+0.2, G332.4−0.4, G354.8−0.8) overlap with the bilateral sample of West et al. (2016).

2.4. MAGPIS

We also considered a sample of 60 SNRs using 1.4 GHz data from the Multi-Array Galactic Plane Imaging Survey (MAGPIS; Helfand et al. 2006). However, we found that the noise in these data led to large uncertainties in the derived power ratios. Thus, we did not use this sample in this paper.

3. Methods

We measure the symmetry of our sample using a multipole expansion technique called the PRM. This technique was developed to quantify the morphologies of galaxy clusters (Buote & Tsai 1995, 1996; Jeltema et al. 2005). Subsequently, it was extended to measure the asymmetries of SNRs in X-ray and infrared images (Lopez et al. 2009a, 2011; Peters et al. 2013; Holland-Ashford et al. 2017). Our work here applies the same technique to radio observations of SNRs. An overview of the method is provided below. For a more detailed description including the mathematical formalism, we refer readers to Lopez et al. (2009a, 2011).

The PRM measures asymmetries by calculating the multipole moments of emission in a circular aperture. It is derived in a similar way to the expansion of a two-dimensional gravitational potential, except an image's surface brightness replaces the mass surface density. The powers P_m are obtained by integrating the magnitude of each term of the multiple expansion over a circle of radius R. We divide the powers P_m by P_0 to normalize with respect to flux, and we set the origin position in our apertures to the geometric centers of the SNR's radio emission. In this case, each term of the multipole expansion reflects asymmetries at successively smaller scales. The dipole power ratio P_1/P_0 represents the bulk asymmetry of the SNR's emission. The quadrupole power ratio P_2/P_0 measures the ellipticity or elongation of a source, and the octupole power ratio P_3/P_0 quantifies the mirror asymmetry.

Before applying the PRM, we removed the point sources from the images by replacing the sources' pixel values with

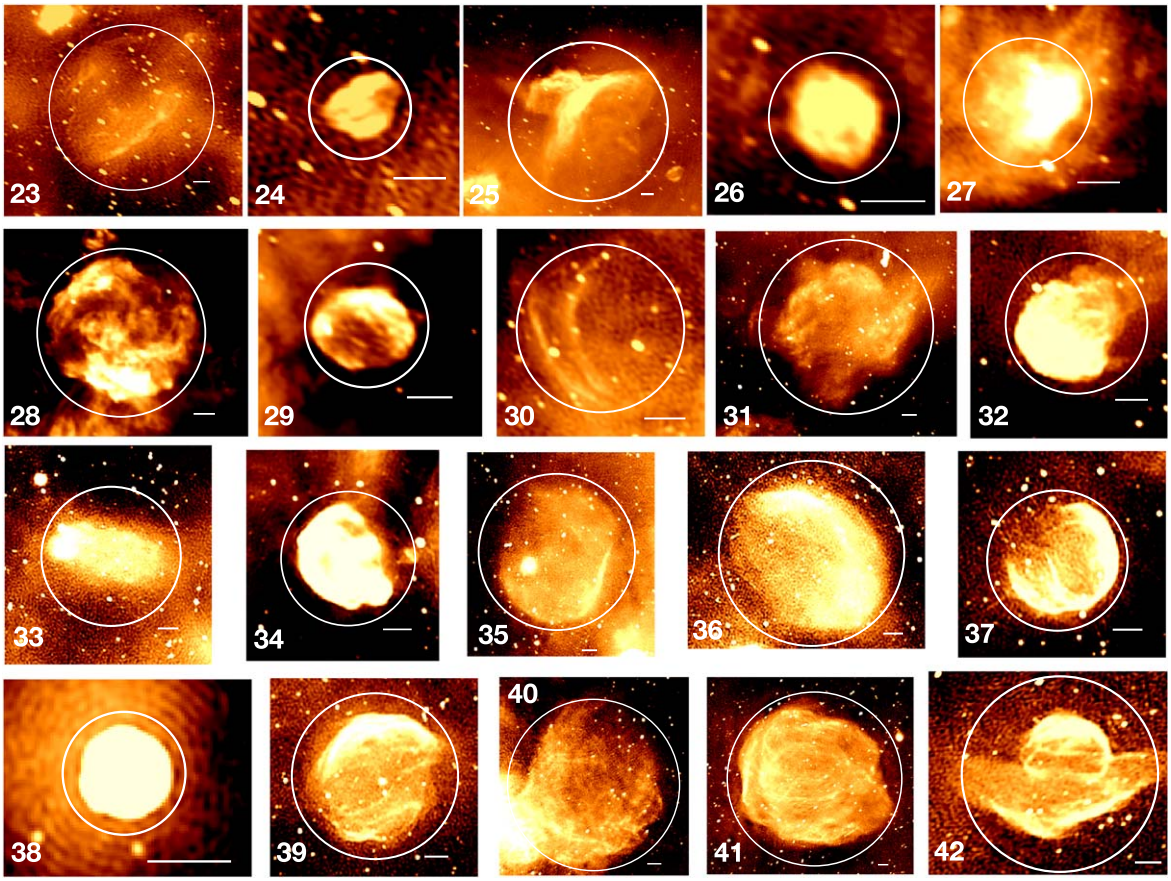

Figure 2. Radio continuum (1.42 GHz) images of 20 SNRs from the CGPS (Kothes et al. 2006) in our sample. The SNRs have radii of 7′–76′. The extents of the sources are marked with white circles, and the white scale bar represents 2′. The numbers correspond to those in Column 1 of Table 2.

those interpolated from surrounding background regions. We determined the SNRs' geometric centers by putting a circle at their right ascensions and declinations reported by Green (2017) and adjusting those positions and sizes to encompass their radio extents. For each SNR, we then ran the PRM on the source and on the adjacent, source-free background and subtracted the background moments from the SNRs' moments.

The selection of the geometric center influences the derived power ratios. For example, we computed the power ratios for G49.2−0.7 (W51C) after shifting the centroid 10 and 20 pixels (25″ and 50″, respectively) from the original analysis to explore the associated uncertainties. The largest effect was on P_1/P_0, which had a 10%–60% (4%–260%) change for the 10-pixel (20-pixel) shift. By comparison, the fractional changes in P_2/P_0 and P_3/P_0 were 2%–16% (5%–38%) and 12%–28% (23%–30%), respectively. These values depend on the direction and magnitude of the offset as well as the substructure and morphology of the individual sources.

The physical resolution (parsecs per pixel)—which depends on the assumed distance to the targets—affects the derived power ratios as well. To demonstrate this point, we calculated the power ratios for G49.2−0.7 (W51C) assuming distances of 0.5–1.5× the estimated distance of 5.4 kpc (i.e., adopted distances of 2.7–8.1 kpc). Shorter distances, corresponding to greater physical resolution, increases the derived power ratios: assuming a distance of 2.7 kpc, the power ratios increased by 43%. At larger distances, the power ratios decrease: a distance of 8.1 kpc produced power ratios that are 22% lower than those listed in Table 1. Thus, the derived power ratios are somewhat sensitive to the adopted distances to the individual targets.

To estimate the uncertainties in the power ratios from noise in the images, we used the Monte Carlo approach as described in Lopez et al. (2009b). Specifically, we smoothed out noise using the program *AdaptiveBin* (Sanders & Fabian 2001), and then we added noise back into the images assuming that each pixel intensity is the mean of a Poisson distribution, and selecting an intensity from that distribution. We repeated this procedure 100 times to create 100 mock images of each source. We ran the PRM on the 100 images, and we calculated the power ratios from the mean of these 100 values. The 1σ confidence limits are derived from the 16 highest and lowest PR values.

4. Results and Discussion

In Figure 4, we plot the dipole power ratio (P_1/P_0; left), the quadrupole power ratio (P_2/P_0; middle), and the octupole power ratio (P_3/P_0; right) versus radius. To convert the radii to parsecs, we adopt the distances listed in Tables 1–3 and the angular extents given in Green (2017).

The sample spans a wide range of power-ratio values, and the median power ratios of the SNRs by radius are listed in Table 4. Generally, SNRs with radii $\lesssim$10 pc have smaller power ratios than those with radii $\gtrsim$10 pc, and this trend is most pronounced in P_2/P_0. We note that 33 of the 96 SNRs have no distance measurements to date (the triangles in Figure 4), and we have assumed a distance of 8.5 kpc to those

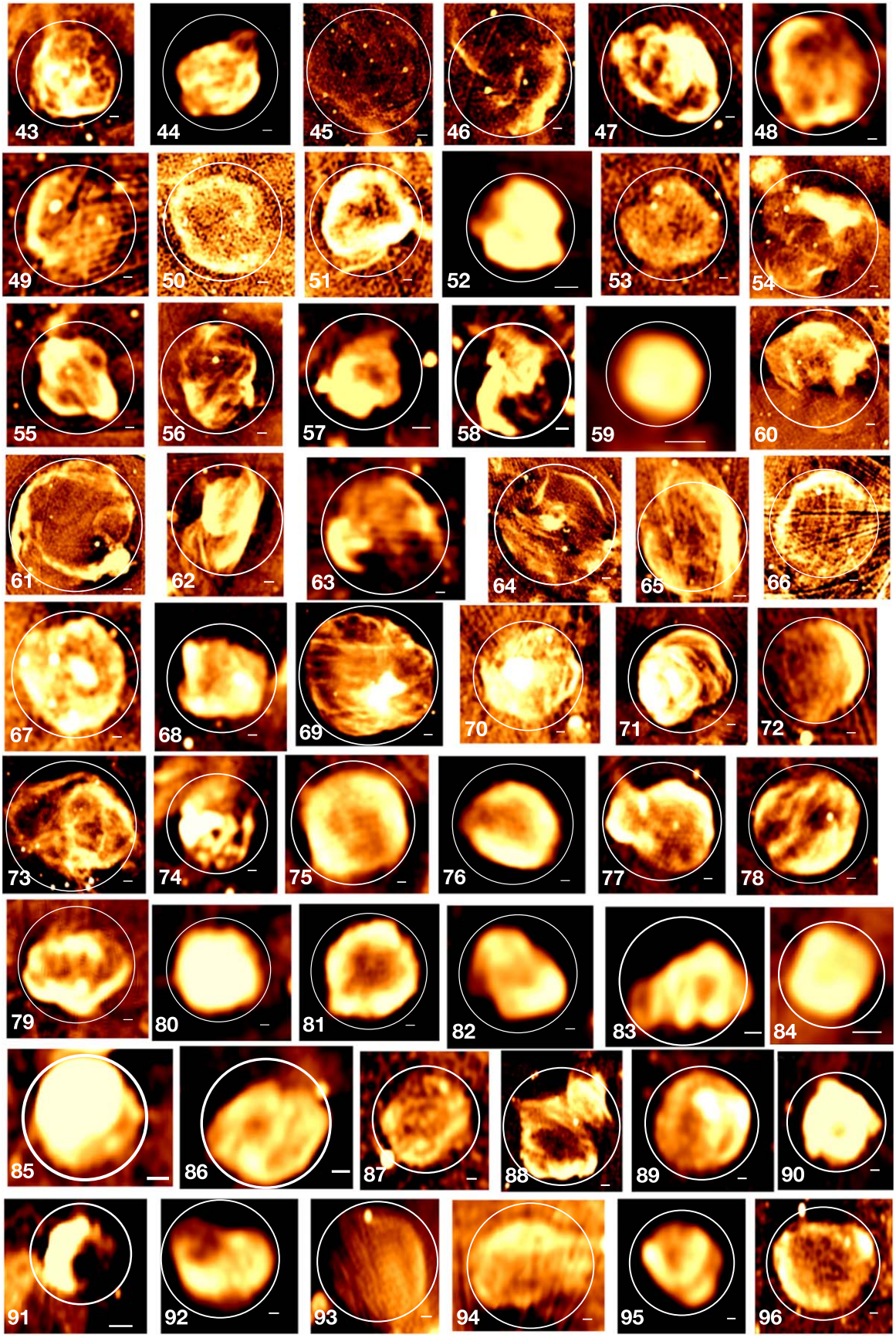

Figure 3. Radio continuum (0.843 GHz) images of 54 SNRs from the MSC (Whiteoak & Green 1996) in our sample. The SNRs have radii of 3′–23′. The extents of the sources are marked with white circles, and the white scale bar represents 2′. The numbers correspond to those in Column 1 of Table 3.

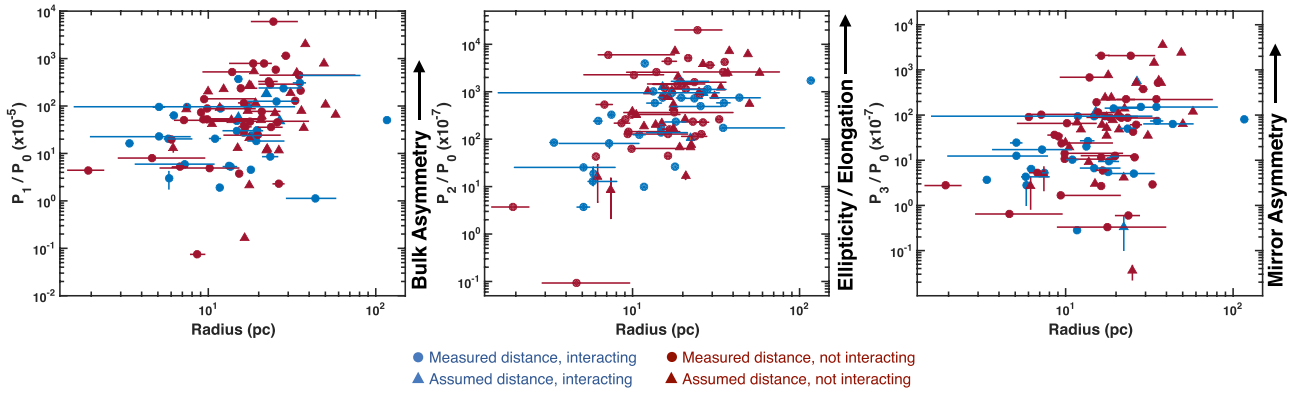

Figure 4. Dipole power ratio P_1/P_0 (left), quadrupole power ratio P_2/P_0 (middle), and octupole power ratio P_3/P_0 (right) vs. radius. P_1/P_0 measures bulk asymmetry, P_2/P_0 quantifies ellipticity/elongation, and P_3/P_0 reflects mirror asymmetries. As shown in the legend, red and blue colors represent whether SNRs have no evidence or some evidence of interaction with molecular clouds, respectively. Symbol shapes denote whether each source has a measured distance in the literature (circles) or no known distance (triangles). Horizontal error bars represent the uncertainty in radii given the sources' distance estimates.

Table 4
Median Power-ratio Results by Radius

Power-Ratio	Radius $\lesssim$ 10 pc	Radius $\gtrsim$ 10 pc
	All 96 SNRs	
P_1/P_0	2.0×10^{-4}	6.7×10^{-4}
P_2/P_0	8.1×10^{-6}	7.5×10^{-5}
P_3/P_0	5.3×10^{-7}	6.8×10^{-6}
	63 SNRs with Measured Distances	
P_1/P_0	2.0×10^{-4}	5.1×10^{-4}
P_2/P_0	8.5×10^{-6}	7.4×10^{-5}
P_3/P_0	6.5×10^{-7}	6.5×10^{-6}

sources. However, if those SNRs are located at closer distances, their power ratios would increase (see Section 3). Thus, we also list the median power ratios of only the 63 SNRs with measured distances in Table 4. We find that this subsample gives similar results, with the smaller SNRs giving lower power ratios, indicative of less asymmetries than the larger SNRs.

Comparing the SNRs associated with Type Ia versus those from core-collapse explosions, G337.2−0.7 and Tycho and have among the lowest power-ratio values among both samples. However, the other Type Ia SNRs have near the median or greater power ratios than the CC SNRs. These results suggest that radio continuum morphology is not a reflection of explosion type, in contrast to X-ray and infrared morphologies where the two classes have distinct symmetries (Lopez et al. 2009a, 2011; Peters et al. 2013). Given that G337.2−0.7 and Tycho have the smallest and third-smallest radii, respectively, of the 96 SNRs in the sample, their symmetric morphologies in the radio may simply reflect their young age and small size.

The radii R_s of the SNRs are a rough proxy of age t, because $R_s \propto t^m$, where m is the expansion parameter, and the shock velocity v_s is given by $v_s = mR_s/t$. The value of m depends on the evolutionary stage of the SNR. During free expansion, $m \sim 1$, and as the shock begins to decelerate, $m \sim 0.6$–0.8 (Chevalier 1982a, 1982b). Once the shock has swept-up a mass M_{sw} that is comparable to the mass of the ejecta M_{ej}, then the SNR enters the Sedov-Taylor (ST) phase, when $m = 0.4$ (Sedov 1959). Subsequently, m decreases from $m = 0.33$ in the pressure-driven snowplow stage (e.g., Blondin et al. 1998) to $m = 0.25$ in the momentum-conserving stage (Cioffi et al. 1988).

Table 5
Ages of the THOR SNRs

Source	R_s[a] (pc)	n_0 (cm^{-3})	M_{SW} ($M_\odot$)	t_{kyr} (kyr)	References[b]
G15.9+0.2	7.4 ± 3.5	0.7	41	2.9[b]	1
G16.7+0.1	5.8 ± 2.3	1.0[c]	28	1.5	…
G18.1−0.1	7.4 ± 0.2	0.6	35	4.4[b]	2
G18.8+0.3	28.1 ± 8.1	1.0[c]	3211	76[c]	…
G20.0−0.2	16.3 ± 0.4	1.0[c]	627	19[c]	…
G20.4+0.1	9.1 ± 4.7	1.0[c]	109	4.5[c]	…
G21.5−0.1	6.2 ± 2.9	1.0[c]	34	1.7[c]	…
G21.8−0.6	$15.1^{+0.0}_{-0.9}$	1.0[c]	498	16[c]	…
G22.7−0.2	16.6 ± 1.5	1.0[c]	662	20[c]	…
G23.3−0.3	17.3 ± 15.7	4.0	2997	45	3
G27.4+0.0	3.4 ± 0.2	0.6	3.4	1.1[b]	4
G28.6−0.1	15.4 ± 0.5	0.2	106	7.5[b]	5
G29.6+0.1	7.3 ± 3.7	1.0[c]	40	2.6[d]	…
G31.9+0.0	6.2 ± 0.3	2.0	69	3.5[b]	6
G32.4+0.1	14.8 ± 3.5	1.0[c]	469	15	…
G32.8−0.1	11.9 ± 9.9	0.1	24	4.2[b]	7
G33.2−0.6	22.3 ± 10.5	1.0[c]	1605	43	…
G33.6+0.1	5.1 ± 0.4	0.4	7.7	3.0[b]	8
G34.7−0.4	13.5 ± 1.4	5.0	1780	10	9
G35.6−0.4	6.8 ± 0.8	1.0[c]	46	2.2	…
G36.6−0.7	30.9 ± 14.5	1.0[c]	4269	96	…
G49.2−0.7	23.6 ± 2.6	0.1	190	18[b]	10

Notes.
[a] The error bars on R_s reflect the uncertainties in the source distances from Table 1. If no uncertainties in distance are given in the literature (or if we have assumed a distance of 8.5 kpc), we assign a distance uncertainty of 4 kpc.
[b] We have scaled the age estimates from the references to the distances listed in Table 1 and the SNR radii in this table.
[c] Assumed $n_0 = 1.0$ cm^{-3} as no constraints on density were found in the literature (Ferrière 2001).
[d] Assumed $E_{51} = 1.0$ as no constraints on explosion energy were found in the literature.

References. (1) Reynolds et al. (2006); (2) Leahy et al. (2014); (3) Castro et al. (2013); (4) Kumar et al. (2014); (5) Bamba et al. (2001); (6) Chen et al. (2004); (7) Zhou & Chen (2011); (8) Sun et al. (2004); (9) Reach et al. (2005); (10) Koo et al. (1995).

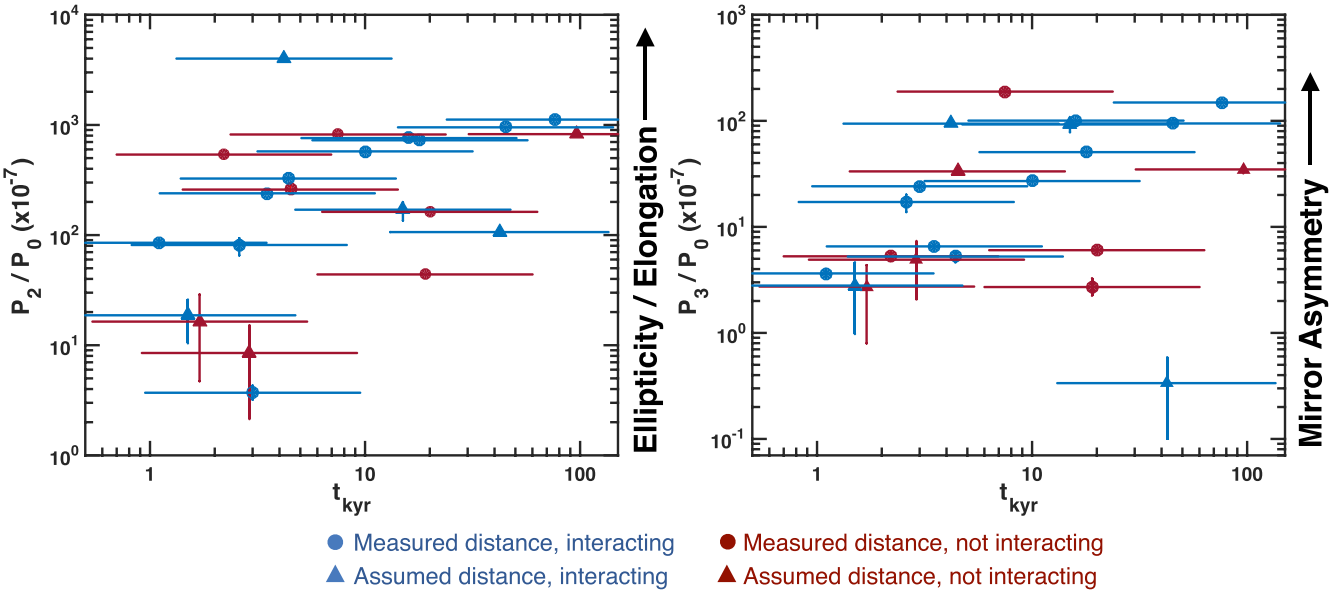

Figure 5. Plots of P_2/P_0 (left) and P_3/P_0 (right) vs. age $t_{\rm kyr}$ (listed in Table 5), assuming the SNRs are in the Sedov-Taylor phase. Error bars on $t_{\rm kyr}$ represent the uncertainty in the ambient density $n_{\rm o}$, which we conservatively assume to be one order of magnitude.

SNR ages are typically derived by assuming that SNRs are in the ST phase of their evolution, the stage that most radio-bright SNRs are thought to be observed (Berkhuijsen 1986; Berezhko & Völk 2004). In this case, ages are determined based on the observed shock velocity by the expression $t = 2R_{\rm s}/5v_{\rm s}$. Alternatively, given an estimate of the mass density of the interstellar medium (ISM) $\rho_{\rm o}$ and the explosion energy E, SNR ages can be derived using the ST solution (Sedov 1959):

$$R_{\rm s} = 1.15\left(\frac{E}{\rho_{\rm o}}\right)^{1/5} t^{2/5} = 5.0\, E_{51}^{1/5} n_{\rm o}^{-1/5} t_{\rm kyr}^{2/5}\ {\rm pc}. \quad (1)$$

On the right side of the equation, E_{51} is the explosion energy in units of 10^{51} erg and $t_{\rm kyr}$ is the SNR age in kyr.

To demonstrate the large uncertainties in age and the challenge of comparing those values to the power ratios, we compiled the age estimates of the THOR SNRs found in the literature (listed in Table 5). When available (e.g., for G15.9+0.2, G32.8−0.1, G33.6+0.1), these values are the dynamical ages derived from the shock radius $R_{\rm s}$ and velocity $v_{\rm s}$, using the relation $t = 2R_{\rm s}/5v_{\rm s}$. For those SNRs without constraints on $v_{\rm s}$, we scale the ages estimated from the ST solution in the references (see Table 5) to the distances in Table 1 and radii in Table 5. For those SNRs without any age estimates in the literature, we adopt the ISM densities $n_{\rm o}$ in Table 5 and assume explosion energies of $E_{51} = 1$ to estimate $t_{\rm kyr}$.

To evaluate the validity of the assumption that all of the SNRs are in the ST phase, we calculated the mass swept-up $M_{\rm SW}$ by their forward shocks: $M_{\rm SW} = \frac{4}{3}\pi R_{\rm s}^3 \times 1.4 m_{\rm H} n_{\rm o}$, where $m_{\rm H}$ is the mass of hydrogen. The resulting $M_{\rm SW}$ for each SNR is listed in Table 5, along with the adopted shock radii $R_{\rm s}$ and ISM densities $n_{\rm o}$ to derive $M_{\rm SW}$. For two SNRs (G27.4+0.0 and G33.6+0.1), $M_{\rm SW} < 10 M_\odot$, and thus their forward shocks may have swept up less than their ejecta masses $M_{\rm ej}$. This result would indicate that they may not have reached the ST phase yet, so their age estimates $t_{\rm kyr}$ in Table 5 are upper limits. Five SNRs (G18.8+0.3, G23.3−0.3, G33.2−0.6, G34.7−0.4, and G36.6−0.7) have $M_{\rm SW} > 10^3 M_\odot$ and thus may have transitioned past the ST phase, which occurs at a time $t_{\rm tr} = 2.9 \times 10^4 E_{51}^{4/17} n_{\rm o}^{-9/17}$ years when the shock has swept up $M_{\rm SW} \approx 10^3 E_{51}^{15/17} n_{\rm o}^{-14/17}\ M_\odot$ (Blondin et al. 1998). In these cases, the age estimates $t_{\rm age}$ should be interpreted as lower limits.

In Figure 5, we plot P_2/P_0 (left panel) and P_3/P_0 (right panel) versus age $t_{\rm kyr}$ of the THOR sample. We find a weak trend that younger SNRs ($\lesssim$3 kyr old) have lower P_2/P_0 and P_3/P_0 than the older SNRs ($\gtrsim$3 kyr old), consistent with the results shown in Figure 4. These findings suggest that SNRs' forward shocks are initially more symmetric, and their expansion into an inhomogeneous medium increases the asymmetries with time. The large dispersion in the power-ratio values in the small/young SNRs indicates that the objects may begin with different degrees of asymmetry as well, possibly reflecting their explosion geometries or the inhomogeneous environments immediately surrounding the SN.

One reason that the plots in Figure 5 show less correlation compared to the power ratios versus radius in Figure 4 may be due to the large uncertainty in the SNR ages. Specifically, the explosion energies and the ISM densities are not well constrained in many cases. For many SNRs, we assumed $n_{\rm o} = 1$ cm^{-3} (as an approximation of the density of the warm neutral medium: Ferrière 2001) and $E_{51} = 1$ due to a lack of any observational constraints. Realistically, these parameters can range from $E_{51} \sim 0.1$–10 (e.g., Sukhbold et al. 2016) and $n_{\rm o} \sim 10^{-3}$–10^2 cm^{-3}. In particular, $n_{\rm o}$ spans several orders of magnitude and depends on the environment of the SNR. If the SNR is expanding into a progenitor's wind bubble, then $n_{\rm o} \sim 10^{-2}$–10^{-3} (e.g., RCW 86: Broersen et al. 2014); if the SNR is interacting with a molecular cloud, then $n_{\rm o} \sim$ 10–100 cm^{-3} (e.g., gamma-ray bright SNRs: Castro & Slane 2010). Generally, $n_{\rm o}$ can be estimated from modeling of X-ray or gamma-ray observations (Castro et al. 2013).

Thus, some age estimates could be off by a factor of ∼10 or more, shifting their placement in Figure 5. Given that the uncertainty in $n_{\rm o}$ is responsible for a large uncertainty in the ages $t_{\rm kyr}$, we compute the error bars of $t_{\rm kyr}$ by calculating the ages for an order-of-magnitude smaller and larger $n_{\rm o}$.

Consequently, the horizontal error bars in Figure 5 are conservative estimates.

Our results are consistent with recent three-dimensional, hydrodynamical simulations of SNRs expanding into an inhomogeneous medium (Kim & Ostriker 2015; Martizzi et al. 2015; Walch & Naab 2015; Zhang & Chevalier 2018). In these works, the authors follow the evolution of SNRs in a multiphase or turbulent ISM. They find that the SNRs in an inhomogeneous medium become progressively more asymmetric compared to those in a homogeneous ISM. For example, Martizzi et al. (2015) showed that the blast wave travels faster in the inhomogeneous medium case, particularly in areas of low-density channels around the SNR. Zhang & Chevalier (2018) found that the mean ambient density is the primary factor influencing SNRs' evolution and that a smoother (lower Mach number) turbulent structure leads to faster, more asymmetric expansion.[8] Thus, the increase in SNR asymmetries with radius (Figure 4) and with age (Figure 5) reflects the inhomogeneous, turbulent structure of the ISM.

We note that Lopez et al. (2009a, 2011) found no age evolution in the power ratios derived from X-ray images of SNRs. However, the soft X-rays trace thermal emission from SNR ejecta, so SNR X-ray morphologies may reflect explosion asymmetries. Furthermore, these previous studies considered only young sources, with ages $t_{\rm kyr} \lesssim 10$, whereas our sample spans a wider range, with $t_{\rm kyr} \sim 1$–100. Further investigation is necessary to determine if size/age evolution is unique to the SNRs' radio continuum morphologies.

To compute ages, we assumed a uniform ambient density, though our results indicate that the SNRs are expanding into inhomogeneous environments (because a homogeneous ISM would lead to no size/age evolution in the asymmetries). Zhang & Chevalier (2018) showed that the mean ambient density is the dominant factor in determining shock expansion with time, though inhomogeneities are important in shaping SNRs overall. Thus, the assumption of a single $n_{\rm o}$ may be sufficient. However, given the large uncertainties in the SNR ages, the radii are the best observable indicators of the SNR evolutionary stage.

In this work, we have analyzed nearly one-third of the SNR population of the Milky Way. In the future, application and comparison to extragalactic SNRs may reveal differences in the turbulent structure of nearby galaxies. While the fractal nature of the Milky Way ISM (Elmegreen & Falgarone 1996) is also observed in nearby galaxies (e.g., in the Small Magellanic Cloud: Stanimirovic et al. 1999), the medium can differ substantially, e.g., in porosity (Bagetakos et al. 2011) or in molecular gas velocity dispersion Sun et al. (2018). Ultimately, comparison of SNRs' morphological evolution with simulations (e.g., Kim & Ostriker 2015; Martizzi et al. 2015; Walch & Naab 2015; Zhang & Chevalier 2018) may place new constraints on the ISM properties of the Milky Way and nearby galaxies.

[8] We note that Martizzi et al. (2015) and Zhang & Chevalier (2018) had different results on the impact of turbulent structure on SNR expansion and morphology. Martizzi et al. (2015) showed that SNRs expand faster in a more turbulent medium, while Zhang & Chevalier (2018) found that smoother turbulent structure leads to faster shock expansion. Zhang & Chevalier (2018) attribute the disparity to how each study models turbulence: Martizzi et al. (2015) used a lognormal density distribution, whereas Zhang & Chevalier (2018) adopted an initial Gaussian velocity perturbation in a uniform medium that grows with time.

We thank Drs. Carles Badenes and Adam Leroy for useful discussions. This work was supported through NSF Astronomy & Astrophysics Grant AST−1517021. L.A.L. acknowledges support from the Sophie and Tycho Brahe Visiting Professorship at the Niels Bohr Institute.

ORCID iDs

Laura A. Lopez https://orcid.org/0000-0002-1790-3148
Katie Auchettl https://orcid.org/0000-0002-4449-9152
Tyler Holland-Ashford https://orcid.org/0000-0002-7643-0504

References

Acero, F., Ackermann, M., Ajello, M., et al. 2016, ApJS, 224, 8
Andersen, M., Rho, J., Reach, W. T., Hewitt, J. W., & Bernard, J. P. 2011, ApJ, 742, 7
Auchettl, K., Slane, P., & Castro, D. 2014, ApJ, 783, 32
Auchettl, K., Slane, P., Castro, D., Foster, A. R., & Smith, R. K. 2015, ApJ, 810, 43
Bagetakos, I., Brinks, E., Walter, F., et al. 2011, AJ, 141, 23
Bamba, A., Sawada, M., Nakano, Y., et al. 2016a, PASJ, 68, S5
Bamba, A., Terada, Y., Hewitt, J., et al. 2016b, ApJ, 818, 63
Bamba, A., Ueno, M., Koyama, K., & Yamauchi, S. 2001, PASJ, 53, L21
Berezhko, E. G., & Völk, H. J. 2004, A&A, 427, 525
Berkhuijsen, E. M. 1986, A&A, 166, 257
Beuther, H., Bihr, S., Rugel, M., et al. 2016, A&A, 595, A32
Blondin, J. M., Wright, E. B., Borkowski, K. J., & Reynolds, S. P. 1998, ApJ, 500, 342
Broersen, S., Chiotellis, A., Vink, J., & Bamba, A. 2014, MNRAS, 441, 3040
Buote, D. A., & Tsai, J. C. 1995, ApJ, 452, 522
Buote, D. A., & Tsai, J. C. 1996, ApJ, 458, 27
Castro, D., & Slane, P. 2010, ApJ, 717, 372
Castro, D., Slane, P., Carlton, A., & Figueroa-Feliciano, E. 2013, ApJ, 774, 36
Castro, D., Slane, P. O., Gaensler, B. M., Hughes, J. P., & Patnaude, D. J. 2011, ApJ, 734, 86
Caswell, J. L., Kesteven, M. J., Stewart, R. T., Milne, D. K., & Haynes, R. F. 1992, ApJL, 399, L151
Caswell, J. L., Murray, J. D., Roger, R. S., Cole, D. J., & Cooke, D. J. 1975, A&A, 45, 239
Chen, Y., Seward, F. D., Sun, M., & Li, J.-T 2008, ApJ, 676, 1040
Chen, Y., Su, Y., Slane, P. O., & Wang, Q. D. 2004, ApJ, 616, 885
Chevalier, R. A. 1982a, ApJL, 259, L85
Chevalier, R. A. 1982b, ApJ, 258, 790
Chomiuk, L., & Wilcots, E. M. 2009, ApJ, 703, 370
Cioffi, D. F., McKee, C. F., & Bertschinger, E. 1988, ApJ, 334, 252
Claussen, M. J., Frail, D. A., Goss, W. M., & Gaume, R. A. 1997, ApJ, 489, 143
De Horta, A. Y., Filipovic, M. D., Crawford, E. J., et al. 2014, SerAJ, 189, 41
Dickel, J. R., Milne, D. K., & Strom, R. G. 2000, ApJ, 543, 840
Dodson, R., Lewis, D., McConnell, D., & Deshpande, A. A. 2003, MNRAS, 343, 116
Doherty, M., Johnston, S., Green, A. J., et al. 2003, MNRAS, 339, 1048
Dubner, G., & Giacani, E. 2015, A&ARv, 23, 3
Dubner, G., Giacani, E., Reynoso, E., & Parón, S. 2004, A&A, 426, 201
Eger, P., Rowell, G., Kawamura, A., et al. 2011, A&A, 526, A82
Elmegreen, B. G., & Falgarone, E. 1996, ApJ, 471, 816
Ferrière, K. M. 2001, RvMP, 73, 1031
Filipovic, M. D., Payne, J. L., & Jones, P. A. 2005, SerAJ, 170, 47
Foster, T. 2005, A&A, 441, 1043
Foster, T. J., Kothes, R., Kerton, C. R., & Arvidsson, K. 2007, ApJ, 667, 248
Frail, D. A., Claussen, M. J., & Méhault, J. 2013, ApJL, 773, L19
Frail, D. A., Goss, W. M., Reynoso, E. M., et al. 1996, AJ, 111, 1651
Frank, K. A., Burrows, D. N., & Park, S. 2015, ApJ, 810, 113
Froebrich, D., Makin, S. V., Davis, C. J., et al. 2015, MNRAS, 454, 2586
Gaensler, B. M. 1998, ApJ, 493, 781
Gaensler, B. M., Manchester, R. N., & Green, A. J. 1998, MNRAS, 296, 813
Giacani, E., Smith, M. J. S., Dubner, G., et al. 2009, A&A, 507, 841
Giacani, E., Smith, M. J. S., Dubner, G., & Loiseau, N. 2011, A&A, 531, A138
Green, A. J., Frail, D. A., Goss, W. M., & Otrupcek, R. 1997, AJ, 114, 2058
Green, D. A. 1984, MNRAS, 209, 449
Green, D. A. 2017, yCat, 7278
Halpern, J. P., & Gotthelf, E. V. 2010, ApJ, 710, 941

Helfand, D. J., Agüeros, M. A., & Gotthelf, E. V. 2003, ApJ, 592, 941
Helfand, D. J., Becker, R. H., White, R. L., Fallon, A., & Tuttle, S. 2006, AJ, 131, 2525
Hewitt, J. W., Rho, J., Andersen, M., & Reach, W. T. 2009, ApJ, 694, 1266
Hewitt, J. W., Yusef-Zadeh, F., & Wardle, M. 2008, ApJ, 683, 189
Holland-Ashford, T., Lopez, L. A., Auchettl, K., Temim, T., & Ramirez-Ruiz, E. 2017, ApJ, 844, 84
Hui, C. Y., & Becker, W. 2009, A&A, 494, 1005
Hui, C. Y., Seo, K. A., Lin, L. C. C., et al. 2015, ApJ, 799, 76
Jackson, M. S., Safi-Harb, S., Kothes, R., & Foster, T. 2008, ApJ, 674, 936
Jeltema, T. E., Canizares, C. R., Bautz, M. W., & Buote, D. A. 2005, ApJ, 624, 606
Jeong, I.-G., Koo, B.-C., Cho, W.-K., et al. 2013, ApJ, 770, 105
Kaspi, V. M., Bailes, M., Manchester, R. N., et al. 1997, ApJ, 485, 820
Kaspi, V. M., Manchester, R. N., Johnston, S., Lyne, A. G., & D'Amico, N. 1996, AJ, 111, 2028
Kawasaki, M., Ozaki, M., Nagase, F., Inoue, H., & Petre, R. 2005, ApJ, 631, 935
Kilpatrick, C. D., Bieging, J. H., & Rieke, G. H. 2016, ApJ, 816, 1
Kim, C.-G., & Ostriker, E. C. 2015, ApJ, 802, 99
Koo, B.-C., Kim, K.-T., & Seward, F. D. 1995, ApJ, 447, 211
Koo, B.-C., & Moon, D.-S. 1997, ApJ, 485, 263
Koralesky, B., Frail, D. A., Goss, W. M., Claussen, M. J., & Green, A. J. 1998, AJ, 116, 1323
Kothes, R., & Dougherty, S. M. 2007, A&A, 468, 993
Kothes, R., Fedotov, K., Foster, T. J., & Uyanıker, B. 2006, A&A, 457, 1081
Kothes, R., & Foster, T. 2012, ApJL, 746, L4
Kothes, R., Uyaniker, B., & Pineault, S. 2001, ApJ, 560, 236
Krause, O., Tanaka, M., Usuda, T., et al. 2008, Natur, 456, 617
Kulkarni, S. R., Predehl, P., Hasinger, G., & Aschenbach, B. 1993, Natur, 362, 135
Kumar, H. S., Safi-Harb, S., Slane, P. O., & Gotthelf, E. V. 2014, ApJ, 781, 41
Landecker, T. L., Pineault, S., Routledge, D., & Vaneldik, J. F. 1989, MNRAS, 237, 277
Lazendic, J. S., & Slane, P. O. 2006, ApJ, 647, 350
Leahy, D., Green, K., & Tian, W. 2014, MNRAS, 438, 1813
Leahy, D., & Tian, W. 2006, A&A, 451, 251
Leahy, D. A., Green, K., & Ranasinghe, S. 2013, MNRAS, 436, 968
Leahy, D. A., & Green, K. S. 2012, ApJ, 760, 25
Leahy, D. A., & Ranasinghe, S. 2012, MNRAS, 423, 718
Leahy, D. A., & Tian, W. W. 2007, A&A, 461, 1013
Leahy, D. A., & Tian, W. W. 2008, AJ, 135, 167
Li, X. H., Lu, F. J., & Li, T. P. 2005, ApJ, 628, 931
Longmore, A. J., Clark, D. H., & Murdin, P. 1977, MNRAS, 181, 541
Lopez, L. A., & Fesen, R. A. 2018, SSRv, 214, 44
Lopez, L. A., Ramirez-Ruiz, E., Badenes, C., et al. 2009a, ApJL, 706, L106
Lopez, L. A., Ramirez-Ruiz, E., Huppenkothen, D., Badenes, C., & Pooley, D. A. 2011, ApJ, 732, 114
Lopez, L. A., Ramirez-Ruiz, E., Pooley, D. A., & Jeltema, T. E. 2009b, ApJ, 691, 875
Lozinskaya, T. A., Sitnik, T. G., & Pravdikova, V. V. 1993, ARep, 37, 240
Martizzi, D., Faucher-Giguère, C.-A., & Quataert, E. 2015, MNRAS, 450, 504
McClure-Griffiths, N. M., Green, A. J., Dickey, J. M., et al. 2001, ApJ, 551, 394
Milne, D. K., & Hill, E. R. 1969, AuJPh, 22, 211
Orlando, S., Bocchino, F., Reale, F., Peres, G., & Petruk, O. 2007, A&A, 470, 927
Park, S., Kargaltsev, O., Pavlov, G. G., et al. 2009, ApJ, 695, 431
Paron, S. A., Reynoso, E. M., Purcell, C., Dubner, G. M., & Green, A. 2006, PASA, 23, 69
Peters, C. L., Lopez, L. A., Ramirez-Ruiz, E., Stassun, K. G., & Figueroa-Feliciano, E. 2013, ApJL, 771, L38
Radhakrishnan, V., Goss, W. M., Murray, J. D., & Brooks, J. W. 1972, ApJS, 24, 49
Rakowski, C. E., Badenes, C., Gaensler, B. M., et al. 2006, ApJ, 646, 982
Rakowski, C. E., Hughes, J. P., & Slane, P. 2001, ApJ, 548, 258
Ranasinghe, S., & Leahy, D. A. 2017, ApJ, 843, 119
Ranasinghe, S., & Leahy, D. A. 2018a, MNRAS, 477, 2243
Ranasinghe, S., & Leahy, D. A. 2018b, AJ, 155, 204
Reach, W. T., & Rho, J. 1999, ApJ, 511, 836
Reach, W. T., Rho, J., & Jarrett, T. H. 2005, ApJ, 618, 297
Reach, W. T., Rho, J., Jarrett, T. H., & Lagage, P.-O. 2002, ApJ, 564, 302
Reach, W. T., Rho, J., Tappe, A., et al. 2006, AJ, 131, 1479
Reynolds, S. P., Borkowski, K. J., Hwang, U., et al. 2006, ApJL, 652, L45
Reynoso, E. M., Green, A. J., Johnston, S., et al. 2004, PASA, 21, 82
Reynoso, E. M., Johnston, S., Green, A. J., & Koribalski, B. S. 2006, MNRAS, 369, 416
Reynoso, E. M., & Mangum, J. G. 2000, ApJ, 545, 874
Rho, J., & Petre, R. 1998, ApJL, 503, L167
Rosado, M., Ambrocio-Cruz, P., Le Coarer, E., & Marcelin, M. 1996, A&A, 315, 243
Routledge, D., Dewdney, P. E., Landecker, T. L., & Vaneldik, J. F. 1991, A&A, 247, 529
Sanders, J. S., & Fabian, A. C. 2001, MNRAS, 325, 178
Sarbadhicary, S. K., Badenes, C., Chomiuk, L., Caprioli, D., & Huizenga, D. 2017, MNRAS, 464, 2326
Sasaki, M., Heinitz, C., Warth, G., & Pühlhofer, G. 2014, A&A, 563, A9
Sasaki, M., Kothes, R., Plucinsky, P. P., Gaetz, T. J., & Brunt, C. M. 2006, ApJL, 642, L149
Sato, T., Koyama, K., Lee, S.-H., & Takahashi, T. 2016, PASJ, 68, S8
Sedov, L. I. 1959, Similarity and Dimensional Methods in Mechanics (New York: Academic Press)
Seta, M., Hasegawa, T., Dame, T. M., et al. 1998, ApJ, 505, 286
Sezer, A., & Gök, F. 2014, ApJ, 790, 81
Shelton, R. L., Kuntz, K. D., & Petre, R. 2004, ApJ, 611, 906
Sollerman, J., Ghavamian, P., Lundqvist, P., & Smith, R. C. 2003, A&A, 407, 249
Stanimirovic, S., Staveley-Smith, L., Dickey, J. M., Sault, R. J., & Snowden, S. L. 1999, MNRAS, 302, 417
Stewart, R. T., Caswell, J. L., Haynes, R. F., & Nelson, G. J. 1993, MNRAS, 261, 593
Su, Y., Yang, J., Zhou, X., Zhou, P., & Chen, Y. 2014, ApJ, 796, 122
Su, Y., Zhang, S., Shao, X., & Yang, J. 2015, ApJ, 811, 134
Sukhbold, T., Ertl, T., Woosley, S. E., Brown, J. M., & Janka, H.-T. 2016, ApJ, 821, 38
Sun, J., Leroy, A. K., Schruba, A., et al. 2018, ApJ, 860, 172
Sun, M., Seward, F. D., Smith, R. K., & Slane, P. O. 2004, ApJ, 605, 742
Sun, M., Wang, Z.-r., & Chen, Y. 1999, ApJ, 511, 274
Taylor, A. R., Gibson, S. J., Peracaula, M., et al. 2003, AJ, 125, 3145
Temim, T., Slane, P., Castro, D., et al. 2013, ApJ, 768, 61
Tian, W. W., Haverkorn, M., & Zhang, H. Y. 2007a, MNRAS, 378, 1283
Tian, W. W., & Leahy, D. A. 2006, A&A, 455, 1053
Tian, W. W., & Leahy, D. A. 2011, ApJL, 729, L15
Tian, W. W., & Leahy, D. A. 2012, MNRAS, 421, 2593
Tian, W. W., & Leahy, D. A. 2013, ApJL, 769, L17
Tian, W. W., Leahy, D. A., & Wang, Q. D. 2007b, A&A, 474, 541
Uchida, H., Koyama, K., Yamaguchi, H., et al. 2012, PASJ, 64, 141
Uyaniker, B., Kothes, R., & Brunt, C. M. 2002, ApJ, 565, 1022
Vasisht, G., & Gotthelf, E. V. 1997, ApJL, 486, L129
Vasisht, G., Gotthelf, E. V., Torii, K., & Gaensler, B. M. 2000, ApJL, 542, L49
Vink, J. 2004, ApJ, 604, 693
Walch, S., & Naab, T. 2015, MNRAS, 451, 2757
Washino, R., Uchida, H., Nobukawa, M., et al. 2016, PASJ, 68, S4
West, J. L., Safi-Harb, S., & Ferrand, G. 2017, A&A, 597, A121
West, J. L., Safi-Harb, S., Jaffe, T., et al. 2016, A&A, 587, A148
Whiteoak, J. B. Z., & Green, A. J. 1996, A&AS, 118, 329
Williams, B. J., Blair, W. P., Blondin, J. M., et al. 2011, ApJ, 741, 96
Winkler, P. F., Williams, B. J., Reynolds, S. P., et al. 2014, ApJ, 781, 65
Yamaguchi, H., Badenes, C., Petre, R., et al. 2014, ApJL, 785, L27
Yamaguchi, H., Tanaka, M., Maeda, K., et al. 2012, ApJ, 749, 137
Yamaguchi, H., Ueno, M., Koyama, K., Bamba, A., & Yamauchi, S. 2004, PASJ, 56, 1059
Yar-Uyaniker, A., Uyaniker, B., & Kothes, R. 2004, ApJ, 616, 247
Zdziarski, A. A., Malyshev, D., de Oña Wilhelmi, E., et al. 2016, MNRAS, 455, 1451
Zhang, D., & Chevalier, R. A. 2018, MNRAS, 482, 1602
Zhang, G.-Y., Chen, Y., Su, Y., et al. 2015, ApJ, 799, 103
Zhou, P., & Chen, Y. 2011, ApJ, 743, 4
Zhou, P., Chen, Y., Safi-Harb, S., et al. 2016a, ApJ, 831, 192
Zhou, X., Chen, Y., Su, Y., & Yang, J. 2009, ApJ, 691, 516
Zhou, X., Yang, J., Fang, M., et al. 2016b, ApJ, 833, 4
Zhou, X., Yang, J., Fang, M., & Su, Y. 2014, ApJ, 791, 109
Zhu, H., Tian, W. W., Torres, D. F., Pedaletti, G., & Su, H. Q. 2013, ApJ, 775, 95